Rain re-evaporation, Boundary layer convection interactions, and Pacific rainfall patterns in an AGCM

Julio T. Bacmeister

Goddard Earth Sciences and Technology Center University of Maryland, Baltimore County, Baltimore, MD 21250

Max J. Suarez

Global Modeling and Assimilation Office, NASA GSFC, Greenbelt, MD 20771

Franklin. R. Robertson

NASA MSFC, Huntsville, AL 35812

Short title:

Abstract. Sensitivity experiments with an atmospheric general circulation model (AGCM) show that parameterized rain re-evaporation has a large impact on simulated precipitation patterns in the tropical Pacific, especially on the configuration of the model's intertropical convergence zone (ITCZ). Weak re-evaporation leads to the formation of a "double ITCZ" during the northern warm season. The double ITCZ is accompanied by strong coupling between precipitation and high-frequency vertical motion in the planetary boundary layer (PBL). Strong re-evaporation leads to a better overall agreement of simulated precipitation with observations. The model's double ITCZ bias is reduced. At the same time, correlation between high-frequency vertical motion in the PBL and precipitation is reduced. Experiments with modified physics suggest that evaporative cooling by rain near the PBL top weakens the coupling between precipitation and vertical motion. This may reduce the model's tendency to form double ITCZs. The strength of high-frequency vertical motions in the PBL was also reduced directly through the introduction of a diffusive cumulus momentum transport (DCMT) parameterization. The DCMT had a visible impact on simulated precipitation in the tropics, but did not reduce the model's double bias in all cases.

1. Introduction

Accurate simulations of tropical precipitation remain a challenge for atmospheric climate models (AGCMs). Basic dynamical issues such as the relationship between low-level convergence and precipitation remain unresolved. Recent studies suggest that intertropical convergence zones (ITCZs) identified using precipitation or outgoing longwave radiation (OLR) may not always correspond with convergence zones identified using satellite surface wind measurements (e.g.; Liu and Xie, 2002). Earlier Hastenrath and Lamb (1977), using ship-based wind observations, also concluded that surface convergence may exist in the absence of precipitation Nevertheless, determining the strength of surface wind convergence in nature remains a challenge. Perhaps as a result of this observational gap little attention has been paid to examining convergence-precipitation coupling in AGCM simulations, even though all the necessary quantities are easily accessible,

A common problem in AGCM precipitation simulations, that may be related to PBL-precipitation coupling, is the so-called double ITCZ bias (e.g.; Meehl and Arblaster, 1998). Many AGCMs form a spurious second ITCZ in the southern hemisphere (8-10°S) under conditions in which observed precipitation is concentrated in a single ITCZ centered around 10 °N. While nature does show hints of a southern ITCZ over the Pacific, particularly during March through May (Zhang, 2001), this feature in AGCMs is usually too strong and persistent, lasting through the northern warm season June-September. The occurrence of double ITCZs in AGCMs leads to large rms errors in simulated precipitation, since it represents a spurious rearrangement of the most intense precipitation on earth. Connections between double ITCZs and other AGCM simulation biases have not been conclusively established. However, it is clearly of concern to climate modelers, if AGCMs are producing large errors in the horizontal distribution of atmospheric latent heating. Finally, the wide distribution and

similar structure of this bias in a variety of AGCMs suggests a the existence of a shared misunderstanding in current implementations of convection parameterizations.

In this study we will examine the connection between PBL convergence and precipitation and the double ITCZ bias in the NSIPP-2 AGCM. A principal motivation for performing this work is a robust sensitivity in the NSIPP AGCM's tropical precipitation to the strength of rain re-evaporation. With stronger rain re-evaporation the model tends toward a realistic single ITCZ configuration. With weak re-evaporation the model produces a strong double ITCZ. This sensitivity has existed in earlier versions of the NSIPP AGCM despite substantially different formulations of re-evaporation. Although this sensitivity has been useful in empirical "tuning" of the NSIPP AGCM to improve precipitation simulations, the physical origin of the sensitivity has not been explained. Anecdotal evidence from other modeling groups suggests that this sensitivity may exist in some form in other AGCMs (I.M. Held, pers. comm.), and also that other sensitivities may exist to parameters such as cumulus friction (Klein et al. 2004).

The goals of this study are to shed light on mechanisms controlling the formation of double ITCZs in the NSIPP AGCM, and to suggest relevant, parameterization-independent diagnostics that can be applied to other AGCM simulations. The paper is organized as follows. Section 2 provides a description of the AGCM used in this study. Section 3 outlines the AGCM experiments performed. Section 4 presents the basic sensitivity of the model simulations to re-evaporation. Seasonal mean fields are shown, as well as some analysis of vertical profiles, re-evaporation tendencies and high frequency transients. Section 5 describes three experiments with modified physics including changes to the vertical profile of re-evaporation cooling, and the addition of a simple diffusive cumulus momentum transport (DCMT) parameterization.

2. Model Description

We use a development version of the NSIPP-2 AGCM (NSIPP-2.0) for this study. NSIPP-2.0 was developed from the NSIPP-1 AGCM, which was documented in Bacmeister and Suarez (2000) and Bacmeister and Suarez (2002). Simulated seasonal means and responses to inter-annual SST variation in NSIPP-1 were both in good agreement with meteorological analyses (e.g.; Schubert et al., 2001, 2002). The significant modifications to NSIPP-2.0 and NSIPP-1 involve the cloud, boundary layer, and convection schemes. These include introduction of a prognostic cloud scheme in place of the Slingo (1987)-type diagnostic scheme used in NSIPP-1, as well as a simple moist boundary layer entrainment scheme, which is called in addition to the existing first-order dry turbulence parameterization of Louis et al (1982). These modifications were aimed at improving the models simulation of subtropical marine stratus decks, and while they also impact simulated precipitation in the tropics, they do not affect the general nature of the ITCZ sensitivities examined in this study. Cloud fields from NSIPP-2 are examined by Zhang et al. (2004).

The dynamical core of NSIPP-2.0 is the same as in NSIPP-1 and is described in Suarez and Takacs (1996). Radiative effects in NSIPP-2.0 are parameterized using the approach of Chou and Suarez (1992). Land surface effects a parameterized according to Koster and Suarez (1996), and orographic wave drag is treated according to Zhou et al. (1996).

2.1 Convection

Convection in the NSIPP AGCM is parameterized according to the relaxed Arakawa-Schubert (RAS) scheme of Moorthi and Suarez (1992). The implementation of RAS in NSIPP-2.0 is modified to include a convective condensate calculation with autoconversion to rain. RAS works by invoking a series of linearly-entraining plumes (or "cloud-types") that detrain at selected levels in the vertical. Consistency is achieved by calculating the entrainment rate necessary to ensure zero buoyancy at the

selected level. These entrainment rates λ are imagined to be roughly related to plume diameter according to λ=0.2/D (Simpson 1971). Other researchers have found improved performance when lower limits are placed on λ, e.g., improved sub-seasonal variability (e.g.; Tokioka et al., 1988; Lee et al. 2003). We use a shear-dependent λ_{min} that varies from around 0.2/2000m under shear free conditions to around 0.2/1250m with a 10 m s^{-1} surface to 700 hPa wind speed change (Bacmeister 2004).

RAS is flexible as far as the number and distribution of plumes or "cloud-types" tested. Our implementation invokes 30 cloud-types per gridbox per physics time-step. These are drawn at random from a uniform distribution in σ. We also emphasize that our implementation does not include an explicit updraft parameterization.

2.2 Prognostic cloud condensate scheme

Our prognostic condensate scheme considers only a single phase of condensate, but tracks two separate species of condensate; a large-scale species $q_{c,LS}$ originating from gridbox condensation and an "anvil" species $q_{c,AN}$ originating from detraining convection. The rationale for this separation is that both the subgrid statistics and the microphysical properties of rapidly processed anvil condensate may be distinct from those of condensate produced by slower, large scale dynamics (e.g. Lawson 2003). The key distinctions in our current scheme are slower autoconversion and higher number densities for $q_{c,AN}$. These higher assumed number densities for $q_{c,AN}$ enter into the optical thickness calculation used by model's radiation scheme. We impose an e-folding time of 3 hours for conversion of $q_{c,AN}$ to $q_{c,LS}$. Convective condensate $q_{c,CN}$ is calculated internally within each RAS cloud-type, but does not interact with the model's radiation calculation.

2.3 Convective autoconversion and re-evaporation

This section gives a brief outline of our parameterization of convective microphysical processes. A more detailed description of our scheme is given in (Bacmeister 2004)

Our basic approach in parameterizing convective microphysical processes is based on a Lagrangian parcel picture. We first estimate an updraft speed for each plume invoked in RAS. This updraft speed combined with the model's vertical grid spacing gives a time interval over which autoconversion is assumed to occur in a given model layer. Autoconversion rates are determined from a nonlinear temperature-dependent expression (Sundquist 1988). This aspect of the convective microphysics is similar to that in Sud and Walker (1999) although we employ a cruder calculation for the convective updraft speed. A profile of precipitating condensate is accumulated over all RAS plumes and then passed to a scheme that accumulates the condensate and also calculates re-evaporation, accretion and surface precipitation fluxes.

The calculation of rain re-evaporation also proceeds according to a Lagrangian viewpoint. An areal fraction for the convective shower is determined based on the estimated total RAS updraft areal fraction, and on local wind shear. Once areal fractions and in-cloud, precipitating condensate mixing ratios are determined, a representative drop size and terminal fall speed are estimated from a Marshall and Palmer (1948) distribution. The drop size gives an evaporation rate, and the fall speed is used to calculate the droplet residence time within the model layer. Roughly speaking, for similar gridbox averaged amounts of precipitating condensate, intense showers occupying a small area will evaporate less than weaker, broader ones. We also allow a fraction of the convective rain shower to be "shielded" from re-evaporation. This is meant to represent rain falling through a saturated environment such as a convective tower or saturated downdraft. In the experiments discussed here this fraction is also shear dependent, with more convective rain shielded from re-evaporation in weak shear environments.

The actual relationship between the shielded fraction and the environmental shear is controlled through a tunable parameter. Two more tunable parameters control the

relationship between updraft areal fraction and shower area, and between shear and shower area. In this study, we control bulk re-evaporation by changing the relationship between shear and shower area, and shielded shower fraction. Experience with previous versions of the NSIPP model suggest that the details of the rain re-evaporation scheme are unimportant in producing the sensitivities discussed here. For clarity we will simply refer to three settings of re-evaporation parameters - weak, moderate, and strong. Details on the formulation of the re-evaporation calculation, as well as parameter values can be found in (Bacmeister et al. 2004)

3. Description of Experiments

We analyze results from 6 experiments (Table 1). The first three of these, denoted B1, B2, and B3, were performed with the same "baseline" model physics, differing only in the choices made for the rain re-evaporation parameters. These experiments were initialized on June 1 1981 from restarts derived from an existing AMIP simulation and and forced with observed SSTs (Reynolds 1996). Exps B1 and B3 ran through December 1987. Experiment B2 was an AMIP style run conducted for the Tropical boundary layer Clouds Climate Process Team and ran through December 1999. For most of the analysis here we will focus on results from 1984 and 1985.

In addition to the three baseline experiments we conducted three experiments with modified or distorted physics. In the first of these - H1 - the cooling produced by rain re-evaporation was redistributed in the vertical as indicated in Figure 1. At each time-step, total mass-weighted re-evaporation cooling below 850 hPa was found and then uniformly applied between 850 and 300 hPa, instead of where originally placed by the re-evaporation scheme. The moistening from re-evaporation was not modified. Thus, moist energy conservation is violated locally, but preserved in a column-integrated sense. The motivation for this experiment was to minimize the direct impact of re-evaporation

on boundary layer dynamics.

The remaining two experiments M1 and M2 employed a simple diffusive cumulus momentum transport (DCMT) scheme devised for GFDL AM2 model (GFDL Global Atmospheric Model Development Team, 2004). The scheme simply enhances K_m proportional to the total local cumulus mass flux diagnosed by RAS. The DCMT scheme has been used in the GFDL model with positive effects on both the simulated precipitation and on the simulated spectrum of ENSO variability in coupled mode. Here we apply DCMT in two experiments; M1, with weak re-evaporation settings as in B1, and M2, with moderate re-evaporation as in B2. Exps H1, M1 and M2 were initialized on Dec 1 1983 and run through Dec 31 1985.

All experiments were conducted at a horizontal resolution of 2×2.5 degrees with 40 unequally spaced σ layers. Extensive suites of diagnostic tendency outputs on σ-surfaces were saved as daily averages, along with standard outputs. These additional diagnostics included most of the significant water substance conversion terms such as moistening by re-evaporating rain, which we denote here by $\mathcal{R}$.

4. Basic Model Sensitivity to Re-evaporation

4.1 Mean seasonal precipitation

Seasonal mean precipitation fields and biases for June-July-August 1984-85 in experiments B1, B2, and B3 are shown in Figures 1 and 2, along with observational estimates of precipitation rates from CMAP (Xie and Arkin, 1997). The results illustrate the important climatological control exerted by the re-evaporation strength in the NSIPP AGCM. Exp B1 with weak re-evaporation (Figs.1a,2a) tends strongly toward a "double ITCZ" configuration, with precipitation rates in excess of 8 mm d^{-1} extending in a narrow, zonally-aligned band along 10S well into the central Pacific. As re-evaporation is strengthened in B2 (Figs. 1b, 2b) and B3 (Figs. 1c, 2c) the double

ITCZ in all three tropical ocean basins becomes less pronounced, although the change in the Pacific basin is most noticeable due to its size. In connection with the weakening of the double ITCZ, a dry bias along the equator in the western Pacific in B1 is also reduced with increased re-evaporation. Overall, the simulations in experiments B2 and B3 appear to be in better agreement with the CMAP climatology. Pattern correlations for the 7-season (1981-87) JJA mean are significantly lower for B1 than for B2 and B3 (Table 1). Wet biases over summertime tropical continents also appear to decrease as rain re-evaporation is strengthened. Over sub-Saharan Africa as well as over the northern Amazon Basin wet biases of over 4 mm d^{-1} exist in Exp B1, while in B3 these regions are nearly bias free.

Unfortunately, not all precipitation biases are reduced by increasing re-evaporation strength in the model. A noticeable deterioration in the simulated precipitation occurs over much of the northern tropical Pacific between Hawaii and southeast Asia (5°N to 20°N and 120°E to 150°W) as re-evaporation increases. Stronger re-evaporation leads to increasing wet biases in this region, culminating in the >8 mm d^{-1} biases evident in the "Phillipine Hotspot" (130°E, 15°N) in Exp B3 (Figs. 1c,2c). This strong wet bias is associated with excessively strong low-level, monsoon westerlies over Indochina, the Phillipines and surrounding ocean. Rain evaporation produces large moist static energy increases just above the PBL because of increased water vapor. Again, with increased evaporation of rainwater more deep convective mass flux is required to offset CAPE production in the PBL. However, in contrast to the ITCZ region, the increased heating tends to amplify the circulation in the monsoon trough and actually enhances CAPE production by moist static energy convergence in the lower troposphere. Moist static energy input to the column increases not only due to strong reductions in net surface radiative flux (due to enhanced greenhouse from water vapor), but also from mass convergence and larger evaporation due to the increased surface winds. In order

to maintain moist static energy balance, the circulation is forced to reconfigure in a skewed fashion with a deep layer of upward vertical motion increases topped by a much stronger, shallower outflow layer. The circulation readjustment in the Monsoon trough over the Phillipines also extends southwestward to the Indian Ocean, producing deleterious effects in the precipitation there. A JJA dry bias in the Indian Ocean also becomes more pronounced with increasing re-evaporation.

We have focused on northern summer because the double ITCZ bias, in models which possess it, is most pronounced during the northern warm season, roughly April-November. During December-February (not shown) some double ITCZ bias remains in our weak re-evaporation simulation. However, overall the DJF precipitation simulations in all 3 experiments are in better agreement with the CMAP climatology.

4.2 Fractional re-evaporation

An important but difficult to observe quantity is the fraction of rain evaporated before reaching the surface. This quantity provides a measure of re-evaporation "strength" that does not depend on the details of the rain re-evaporation parameterization used. Figure 3 shows maps of the fraction

$$f = \frac{\int \mathcal{R}}{\mathcal{P}}$$

that is the ratio of the vertical mass integral of re-evaporation tendency to surface precipitation flux. The figure shows that in Exp B1 values of f are below 1 almost everywhere, except over arid continental regions. In Exps B2 and B3 the re-evaporation fraction increases dramatically. In both experiments values of f are over 1 across most of the tropics and subtropics. Only stratocumulus regions show values of f below 1 in these simulations. In Exp B3 most of the Indian Ocean is characterized by f close to or exceeding 2. That is, over twice as much rain evaporates during its fall through the atmosphere, as makes it to the surface. The area of the southern Pacific ITCZ exhibits

similar values of f.

Table 2 lists domain averages of $\mathcal{P}_0$, $\int \mathcal{R}$ and other quantities in the box shaped domains shown in Figure 4. The domain averaged precipitation in the central southern Pacific ITCZ (domain "SITCZ") for the baseline experiments varies from just over 6.1 mm d^{-1} in B1 to just under 4 mm d^{-1} in B3. By comparison the surface evaporation E_0 (column 8) varies little from experiment to experiment, hovering between 5.2 and 5.4 mm d^{-1} in SITCZ. The difference $E_0 - \mathcal{P}_0$ (last column) is the implied transport water vapor in or out of each domain, with negative numbers implying a net horizontal transport into the domain. Domain SITCZ is a net water vapor sink in Exp B1, but becomes a net source with stronger rain re-evaporation in B2 and B3. For the strongest re-evaporation tried (B3), both ITCZ domains become net sources of water vapor.

Results for two warm season continental domains are also shown: an arid one containing the southwestern US "WUSA"; and a moist one containing the West African ITCZ region "WAFR". Despite large differences in the amounts of precipitation and in the fractions of re-evaporated rain, these continental domains exhibit a interesting similarities in their sensitivity to re-evaporation. Both rain and surface evaporation decrease markedly with increasing rain re-evaporation. This is in contrast to the situation over ocean (SITCZ and NITCZ) where surface evaporation is largely unaffected by rain re-evaporation. Note the large values of f (column 6, Table 2) in WUSA for all experiments. These may be related to the lack of an explicit downdraft parameterization in the model.

Observational estimates of domain averaged precipitation from CMAP are also shown in Table 2. Comparisons of these with the simulation results tend to confirm that Exp B2 possesses the "best" precipitation, as implied by the pattern correlations and normalized variances in Table 1. Comparison of observations and simulations in WUSA show that our model has a pronounced dry bias in this region, probably related

to excessive re-evaporation of rain. Unfortunately, global observational estimates of $\int \mathcal{R}$ are not currently available.

4.3 Vertical profile of Rain Re-evaporation

Figure 5 shows seasonal mean profiles of re-evaporation tendency $\mathcal{R}$, horizontally-averaged within Box NITCZ. This boxes straddles the northern ITCZ during JJA. Re-evaporation in Exps B2 and B3 is generally strong (1 to 2 g kg^{-1} d^{-1}) throughout the lowest 500 hPa of the atmosphere. A minimum in $\mathcal{R}$ occurs in the upper portion of the model PBL where relative humidities are high, but both within the PBL and immediately above the PBL-top re-evaporation is high. It is worth noting that the re-evaporation profile in Exp B1 is dominated by large-scale and anvil showers, which are assumed to be unaffected by the shear-dependent, re-evaporation parameters varied in this study.

Re-evaporation of condensate is not a process for which we have direct observational data to validate models. On the other hand, TRMM radar precipitation rate profiles have shapes that show evidence of the precipitation process and provide a strong constraint on precipitation evaporation. In Figure 6 we show separate tropical mean profiles averaged for oceanic and land areas for experiments B1 and B2. Here model anvil and grid-scale precipitation is added together and denoted as "stratiform" for comparison to TRMM data. The partitioning between stratiform and convective rainfall for TRMM is not reported at the surface, so we have estimated this by partitioning the TRMM surface rain in the same fraction as is reported at the 2 km level. We note immediately that TRMM surface precipitation is substantially lower than our simulated precipitation, by up to 33%. Our annually-averaged tropical and global mean surface precipitation rates are in reasonable agreement with CMAP values: 2.9 mm d^{-1} simulated global mean vs. 2.7 mm d^{-1} in CMAP, and 3.2 mm d^{-1} simulated

tropical mean vs. 3.1 mm d^{-1} in CMAP. Substantial differences between observational precipitation estimates still exist. In any case our comparison here will focus on the qualitative aspects of the profiles.

Over ocean we notice distinct differences in the model and TRMM vertical profiles: (i) TRMM profiles have a more equal partitioning of stratiform and convective rain but the model has far greater percentage of rain from convective cells. Convective rainfall at low levels appears too large in the lower troposphere. This is especially true of the low evaporation experiment, B1. (ii) The relative amount of precipitation at upper levels (p<500 mb) appears far greater in the model than in TRMM. This is especially true of the stratiform component. In fact, the increased evaporation experiment, B2, exacerbates the disagreement with TRMM. (iii) The shape of the model stratiform profile also differs from TRMM in that below the freezing level ($p\approx$550 hPa), precipitation decreases whereas TRMM stratiform rain rates continue to increase slightly. (iv) At the surface, changing evaporation efficiency has only a very small effect over the oceans and a somewhat larger effect over land. Over land, many of the same patterns remain, especially the excessive stratiform precipitation at upper levels.

These differences suggest that just altering precipitation evaporation will not be sufficient to produce a correct model precipitation climatology and at the same time produce a water budget that agrees with TRMM observations. Other aspects of the bulk microphysical microphysical processes, such as cloud autoconversion rates, are inconsistent with the observations. Furthermore, other processes in the convective parameterization may not be realistic. The lack of convective scale downdrafts may contribute to the large fraction of convective precipitation at low levels. It should also be kept in mind that the accuracy of TRMM rainfall profiles above the freezing level is subject to far more uncertainty than in below where hydrometeors are all liquid. Unknown hydrometeor particle shapes, ice density, and the extent of mixed

phase precipitation combine to make accurate determinations of frozen hydrometeor precipitation rates difficult and errors up to a factor of 2 might be possible in stratiform rain rates. Even with this conservatively large error estimate, the model rainfall rates at upper levels are thought to be excessive.

4.4 Water vapor distribution

The re-evaporation profiles shown in Fig 5 have an impact on the water vapor distribution in the atmosphere. Figure 7 shows mean water vapor profiles for Exps B1-B3 in boxes SITCZ and NITCZ along with estimates from NCEP (Kalnay et al., 1995)and ERA40 (Simmons and Gibson, 2000) re-analyses. In NITCZ (Fig. 7,top) the two re-analyses disagree by nearly 3 g kg^{-1} over much of the layer between below 300 hPa. The three model experiments generally lie in between the two re-analysis profiles. The profile for Exp B3 is up to 2 g kg^{-1} wetter than that for B1 with the largest differences centered around 700 hPa. The profile for B2 lies between those for B1 and B3. In Box SITCZ (Fig. 7, bottom) the situation is somewhat different. The q-profiles from our 3 model experiments are quite similar to the corresponding profiles in NITCZ, with B3 the wettest, B1 the driest, and B2 in the middle. The NCEP re-analysis profile in SITCZ is also similar to that in NITCZ. However, the ERA40 re-analysis profile is significantly drier, and here agrees closely with the NCEP profile. Generally speaking it is clear that increasing re-evaporation in our model leads to mid-tropospheric moistening. However, the differences in q-profiles for different re-evaporation strength appear to be comparable to uncertainties in re-analysis q-profiles. Comparison with SSMI total precipitable water (TPW) measurements (not shown) exhibit a small but worsening global mean wet bias as re-evaporation increases from B1 to B3, although the spatial distribution of simulated TPW improves.

4.5 Relation of low-level convergence and Rainfall

The strength of the high-frequency coupling between low-level flow convergence and precipitation in nature is still not well known (e.g. Gu and Zhang, 2002). However, there are indications that the connection between low-level convergence and precipitation at time-scales of several days and shorter may not be as strong as commonly assumed. We examine this coupling in our simulations by looking at the correlation of daily ω at 850 hPa $\omega_{850}(d)$ with daily rainfall $\mathcal{P}(d)$ in our simulations. Straightforward time-series correlations are calculated at each model gridpoint using results from the 366-day combined period April 1-September 30, 1984 and 1985 A 31-day, high pass Lanczos filter (Duchon 1979) was first applied to each period to remove low-frequency variability. Figure 8 shows maps of the correlation $r(\omega_{850}, \mathcal{P})$ for Exps B1, B2, There is a pronounced difference in the strength of this correlation as re-evaporation changes. For weak re-evaporation as in B1 (Fig. 8a) the correlations are over 0.8 over much of the tropical Pacific. By contrast, with strong re-evaporation as in B3 (Fig. 8c), correlations are generally between 0.4 and 0.6, and fall below 0.4 over large portions of the warm pool and the southern ITCZ region (0-10°S, 180-150°W). A strong reduction in $r[\omega_{850}(d), \mathcal{P}(d)]$ is notable along the equator in the western Pacific as re-evaporation increases.

We examine the strength of the underlying dynamical variability by looking at the rms amplitude of $\omega_{850}(d)$ fluctuations (Figure 9) Maps of $\sqrt{\overline{\omega_{850}(d)^2}}$ show that the pattern of dynamical variability is not straightforwardly related to the correlation patterns in Fig. 7. For example, $\sqrt{\overline{\omega_{850}(d)^2}}$ over the northern warm pool and western tropical Pacific (0-20°N, 120°E-180°E) is similar in B1, B2 and B3 with values around 50-70 hPa d^{-}1. However, $r[\omega_{850}(d), \mathcal{P}(d)]$ in the same region varies from 0.6 to >0.8 in B1 to <0.4 in B3. Interestingly, this is the region in which larger re-evaporation appears to lead to a strengthening wet bias. It appears safe to conclude that this bias, and precipitation generally, in this region is not controlled principally by boundary

layer/precipitation interactions. By contrast, over both ITCZ regions the dynamical variability weakens systematically as re-evaporation increases. This is especially true west of 150°W, where, for example, B1 shows values of $\sqrt{\overline{\omega_{850}(d)^2}}$ of 60 to 80 hPa $d^{-}1$, and B3 shows values of 30 to 50 hPa $d^{-}1$. Variability in the southern ITCZ is especially sensitive to increasing re-evaporation. These results strongly suggest that feedback amplification of transient disturbances is responsible for maintaining ITCZ precipitation in our model.

We have not attempted a detailed comparison of our simulated x-t spectra of rainfall or vertical motion with observations (e.g.; Wheeler and Kiladis, 1997; Gu and Zhang, 2001). However, a cursory look at our model's background spectra of precipitation along the ITCZ suggest at least a qualitative resemblance with the background OLR spectra in Gu and Zhang (2001).

5. Experiments with Altered Physics

5.1 Vertically-redistributed Re-evaporation cooling

From the results shown in Section 4 we speculate that the formation of ITCZs in our simulations is driven by strong coupling between boundary layer convergence and precipitation. The disappearance of double ITCZs with increased re-evaporation lead us to speculate further that this coupling is interrupted by evaporative cooling near the top of the PBL. To test these hypotheses, we performed an experiment, H1 (Table 1), in which we arbitrarily removed cooling driven by rain re-evaporation below 850 hPa. This experiment used "strong" re-evaporation settings as in B3. To conserve at least column-integrated moist static energy, we calculated a mass-weighted integral of the re-evaporation cooling between 850 hPa and the surface before removing it. This mass-weighted cooling was then redistributed uniformly between 300 and 850 hPa. The corresponding moistening profile was not altered. The motivation for this procedure

was to remove the low-level cooling from rain re-evaporation while retaining the lower tropospheric moistening.

Figure 10a shows seasonal mean JJA 1984-85 precipitation from H1. A strong double ITCZ re-appears in this experiment even though re-evaporation parameters are as in Exp B3 (Fig.1c,2c). In fact, Figure 8b shows that the fraction of re-evaporated rain is generally higher than in B3. Domain averages of precipitation and re-evaporation related quantities for H1 are shown in Table 2. Figure 10c shows the correlation of $r[\omega_{850}(d), \mathcal{P}(d)]$ for H1. Comparison with the same quantity for Exps B1, B2, and B3 (Fig. 8) reveals that that $r[\omega_{850}(d), \mathcal{P}(d)]$ is as high in H1 as it was in B1. Thus, this experiment suggests that the low-level cooling associated with rain re-evaporation does in fact disrupt positive feedback between low-level convergence and precipitation. Artificially removing the low-level cooling from an experiment with strong re-evaporation restores the feedback and leads to the re-appearance of strong double ITCZ bias in the model.

5.2 Diffusive Cumulus Momentum Transport (DCMT)

As described in the introduction, the simulation of tropical precipitation in other AGCMs may exhibit sensitivities to other processes. The GFDL AGCM has shown a strong sensitivity to the presence of a diffusive cumulus momentum transport parameterization (Klein et al., 2004). The GFDL DCMT scheme is formulated as a momentum diffusivity proportional to the total cumulus mass flux passing through a given level. Its effects are largest at low-levels where all clouds, both weakly entraining deep clouds, as well as strongly entraining shallow clouds are present. When DCMT is present in GFDL model, the simulated tropical precipitation is improved, in particular the model's tendency to form double ITCZs is reduced. This may be consistent with the picture obtained above in that the net effect of high-frequency features in PBL convergence on precipitation can be reduced indirectly, by disrupting the coupling

between these processes as above, or directly, by reducing the amount of high frequency variability in PBL convergence, as could happen with the introduction of strong cumulus friction.

We performed two experiments with DCMT (Table 1). One, M1, used re-evaporation parameters as in B1. In the baseline model these parameters led to a pronounced double ITCZ bias (Figs. 1a, 2a) The second experiment with DCMT, M2, used re-evaporation parameters as in B2. In the baseline model these parameters produced a reasonable simulation of precipitation overall, with a weak double ITCZ bias (Figs 1b,2b). First, we examine the magnitude of high frequency variability in M1 and M2 compared with that in the corresponding experiments without DCMT. Figure 11 shows the JJA 1984-85 seasonal mean rms value of ω averaged in a band from 155°E to 130°W for Exps B1, B2, M1 and M2. The addition of DCMT clearly reduces the magnitude of ω fluctuations compared with the baseline experiment using the same re-evaporation parameters. Nevertheless, the ω fluctuations in M1 are still larger in the southern ITCZ region 10°S than the fluctuations in B2. This suggests the dissipative effects of DCMT are being overwhelmed by feedbacks between moist heating and PBL convergence.

The 1984-85 JJA mean precipitation for Exps M1 and M2, is shown in Figures 12a and 12c. The small double ITCZ bias in Exp B2 is further reduced by the added DCMT in M2, although the wet bias in the northwestern tropical Pacific (Eq-20°N, 120°E-180) appears to have been exacerbated, much as in Exp B3. On the other hand the strong double ITCZ bias in the Pacific in B1 is not qualitatively reduced by the added DCMT in M1. There are a number of subtle differences between precipitation fields in M1 and B1. The northern ITCZ in M1 is somewhat weaker and more diffuse looking than in B1, particularly in the eastern Pacific between 150°W and 120°W. Nevertheless, a strong, well developed spurious ITCZ persists in the Pacific around 10°S from 150°E to around

130°W. Interestingly, in the Atlantic, there is a more distinct reduction in the double ITCZ bias in Exp M1.

The correlation $r[\omega_{850}(d), \mathcal{P}(d)]$ (Figures 12b and 12d) shows slight increases with added DCMT primarily along the eastern margins of the Pacific ITCZs. and also in the dry band along the Equator. In regions of strong precipitation $r[\omega_{850}(d), \mathcal{P}(d)]$ appears relatively insensitive to DCMT. Thus, changes in precipitation patterns between B1 and M1 or B2 and M2 are not brought about by changes in the coupling strength of the PBL-precipitation coupling.

6. Joint Probability Density Functions (PDFs) of Precipitation and ω

Correlation coefficients quantify the "goodness" of a particular (linear) functional relationship between two variables. A more general graphical alternative to assessing such a relationship is to construct a joint PDF of the quantities in question. PDFs can provide a concise graphical picture of phenomena involving complicated nonlinear variability (e.g.; Sparling 2000). We construct joint PDFs of ω_{850} and $\mathcal{P}(d)$ using all gridbox daily mean values for the period April 1-September 30 in 1984 and 1985, contained within Box SITCZ (Fig. 4). We simply sort the values into 2D bins of 5 hPa d^{-1} for ω_{850} and 1 mm d^{-1} for $\mathcal{P}(d)$. Occurrences n in each bin are counted. We then determine values of n that enclose 95, 90, 80, 66, 50, and 33% of the total data. Note that as the percentage of data enclosed decreases, n increases. Results are shown in Figure 13, with $n > n_{80}$ hatched to emphasize the "core" region of the PDF.

The PDFs concisely display several interesting features of the high-frequency variability in our experiments. First, note the overall similarity in the magnitude of variability in the baseline experiments B1, B2, and B3, as implied by the degree of scatter about the main PDF crests or ridge-lines. Nevertheless, clear differences in the

shapes of the PDFs exist. An increasingly diffuse relationship exists between ω_{850} and $\mathcal{P}(d)$ as re-evaporation strength increases, consistent with the time-series correlations obtained for B1, B2 and B3 (Fig. 8) Comparing B3 (Fig. 13c) and B2 (Fig. 13b) with B1 (Fig. 13a) or M2 (Fig. 13f) with M1 (Fig. 13e) we see that re-evaporation decorrelates ω_{850} and $\mathcal{P}(d)$ primarily by populating the sectors associated with strong precipitation and weak or downward vertical motion near the top of the PBL. Sectors corresponding with strong upward ω_{850} and weak precipitation remain relatively empty in all experiments.

The PDFs also clearly illustrate the impact of DCMT on the simulations. For weak re-evaporation, Exps B1 and M1, relatively tight relationships between ω_{850} and $\mathcal{P}(d)$ exist, with similar sensitivities $\frac{\partial \mathcal{P}(d)}{\partial \omega_{850}}$ indicated by slope of the PDF cores. Instead, the main effect of DCMT in both M1 and M2 is to greatly reduce the spread of the PDFs at low values of n, while the area of the core regions is relatively unaffected, when compared with PDFs from the corresponding DCMT-free experiments. In other words, the proportion of extreme events is reduced. It is of interest that this occurs even for the weak ω_{850}/ strong $\mathcal{P}(d)$ sectors of B2 and M2.

7. Summary and Discussion

We examined the effect of rain re-evaporation and cumulus friction parameterizations on the coupling between upward motion near the top of the PBL ω_{850} and precipitation$\mathcal{P}_0$ in a series of AGCM experiments. We found that stronger rain re-evaporation leads to reductions in the double ITCZ bias in our model's simulated precipitation. The effect of rain re-evaporation on seasonal mean precipitation appears to be at least partially due to low-level evaporative cooling, which prevents feedbacks between convective heating and PBL convergence. This is evident in decreased correlations between time series of vertical motion at 850 hPa ω_{850} and time series of precipitation throughout the Pacific

ITCZ region. An experiment in which re-evaporative cooling was eliminated below 850 hPa, yielded an intense double ITCZ, and high ω_{850}-$\mathcal{P}_0$ correlations, despite large column integrated re-evaporation moistening. Experiments with a simple diffusive Cumulus momentum transport scheme (DCMT) were encouraging in that they suggested the Pacific ITCZs will respond directly to a reduction in dynamical variability in the tropics. However, the increased dissipation provided by DCMT was not enough in our model to counteract feedback between $\mathcal{P}_0$ and ω_{850} for weak re-evaporation. So that double ITCZ biases could persist with DCMT present.

Recently, Wu et al. (2003) have shown improvement in CCM3's simulated seasonal evolution of the ITCZ, when a CMT scheme (Zhang and Cho, 1993) was introduced. The relationship of those results to the present study are not yet clear. However, it is of interest that some form of CMT is found to alleviate tropical precipitation biases in two different AGCMs.

Gu and Zhang (2001) categorize theories of ITCZ formation in to two broad categories 1) SST forced, and 2) internally forced by atmospheric dynamics. Category (2) is further divided into zonally-symmetric and zonally-asymmteric theories. In our model, the connection of high-frequency variability in PBL-top vertical motion with ITCZ precipitation is suggestive of the wave-driven dynamical mechanisms proposed by Holton et al. (1971), Chang (1973) and Lindzen (1974), and later examined in Aquaplanet GCM simulations by Hess et al. (1991).

However, the focus of this paper is not to explain the mechanisms behind the formation of spurious double ITCZs in climate models. Instead, we encourage modelers to examine a number of relatively-simple, parameterization-independent diagnostics that may yield new dynamically-significant similarities between models that suffer similar precipitation biases. Example of such diagnostics examined here include; the ratio of re-evaporated rain to rain reaching the surface, profiles of domain-averaged

re-evaporation moistening, and the correlation of high-frequency time series of vertical motion and precipitation. This list is certainly insufficient, but we believe more detailed examination of atmospheric water budgets and high-frequency precipitation and dynamical variability in climate models is called for despite the relatively poor observational basis available for validation.

References

Bacmeister, J. T., P. J. Pegion, S. D. Schubert, and M. J. Suarez, 2000: Atlas of seasonal means simulated by the NSIPP-1 atmospheric GCM, *NASA Technical Memorandum 104606*, **17**, 194pp.

Bacmeister, J. T. and M. J. Suarez, 2002: Wind Stress simulations and the equatorial momentum budget in an AGCM. *J. Atmos. Sci.*, **59**, 3051–3073.

Bacmeister, J. T. and M. J. Suarez, 2004: Description of moist-process parameterizations in the GEOS5 AGCM. (in preparation). equatorial momentum budget in an AGCM. *J. Atmos. Sci.*, **59**, 3051–3073.

Chou, M.-D. and M. J. Suarez, 1994: An efficient thermal infrared radiation parameterization for use in general circulation models. NASA Technical Memorandum, 104606, **10**, 84pp.

Duchon, C. E., 1979: Lanczos filter in one and two dimensions. *J. Applied Meteor.*, **18**, 1016-1022.

Gu, G., and C. Zhang 2001: A spectrum analysis of synoptic-scale disturbances in the ITCZ. *J. Climate*, **14**, 2725-2739.

Gu, G., and C. Zhang 2002: Westward-propagating synoptic-scale disturbances and the ITCZ. *J. Atmos. Sci.*, **59**, 1062-1075.

Hess, P. G., D. S. Battisti, and P. J. Rasch, 1993: Maintenence of the intertropical convergence zones and the large scale tropical circulation on a water-covered earth. *J. Atmos. Sci.*, **50**, 691-713.

Holton, J. R., J.M. Wallace, and J. A. Young, 1971: On boundary layer dynamics and the ITCZ, *J. Atmos. Sci.*, **28** 275-280.

Kalnay, E., M. Kanamitsu, R. Kistler, W. Collins, D. Deaven, J. Derber, L. Gandin, S.

Sara, G. White, J. Woollen, Y. Zhu, M. Chelliah, W. Ebisuzaki, W. Higgins, J. Janowiak, K. C. Mo, C. Ropelewski, J. Wang, A Leetma, R. Renolds, R Jenne, 1995: The NMC/NCAR reanalysis project. *Bull. Am. Met. Soc.*, **77**, 437-471.

Klein, S. A., and GFDL Atmospheric Model Development Team, 2004: The new GFDL global atmospheric and land model AM2/LM2: Evaluation with prescribed SST simulations, (*J. Climate,* **to appear).**

Koster, R. D., and M. J. Suarez, 1996: Energy and water balance calculations in the Mosaic LSM. *NASA Technical Memorandum 104606*, **9**, 69pp.

Lawson, P., 2003: A comparison of microphysical properties of wave, cirrus and anvil clouds., CRYSTAL-FACE Science Team Meeting, Feb. 2003, (http:/cloud1.arc.nasa.gov/crystalface/presentations_files/250p_Lawson.pdf)

Lee, M-I., I-S. Kang, and B. E. Mapes, 2003: Impacts of cumulus convection parameterization on aqua-planet AGCM simulations of tropical intraseasonal variability. *J. Meteor. Soc. Japan*, 81, 963-992.

Lindzen, R. S., 1974: Wave-CISK in the tropics, *J. Atmos. Sci.*, **31**, 156-179.

Louis, J., M. Tiedtke, J. Geleyn, 1982: A short history of the PBL parameterization at ECMWF, in *Proceedings, ECMWF Workshop on Planetary Boundary Layer Parameterization, Reading, U. K.*, p59-80.

Marshall, J. S., and W. M. Palmer, 1948: The distribution of raindrops with size. *J. Meteor.*5,165-166.

Moorthi, S., and M. J. Suarez, 1992: Relaxed Arakawa-Schubert: A parameterization of moist convection for general circulation models. *Mon. Weather Rev.*, **120**, 978-1002.

Reynolds, R. W., 1988: A real-time global sea surface temperature analysis. *J. Climate,* **1**, 75-86.

Schubert S. D., M. J. Suarez, Y. H. Chang, and G. Branstator, The impact of ENSO on extratropical low-frequency noise in seasonal forecasts. *J. Climate,* **14**, 2351-2365, 2001.

Schubert S. D., M. J. Suarez, P. J. Pegion, M. A. Kistler, and A. Kumar, Predictability of zonal means during boreal summer. *J. Climate,* **15**, 420-434, 2002.

Simpson, J., 1971: On cumulus entrainment and one-dimensional models. *J. Atmos. Sci.,* **28**, 449-455.

Slingo, J., 1987: The development and verification of a cloud prediction scheme for the ECMWF model. *Quart. J. Roy. Meteor. Soc.* , 113, 899-927

Simmons, A. J., and J. K. Gibson, 2000: The ERA-40 project plan *ERA-40 Project Series No. 1*, ECMWF Publications, Reading, U. K.

Sparling,L. C., 2000: Statistical Perspectives on Stratospheric Transport. *Rev. Geophys.,* **38**, 417-436.

Suarez, M. J. and L. L. Takacs, 1995: Documentation of the Aries/GEOS dynamical core Version 2. *NASA Technical Memorandum 104606*, **10**, 56pp.

Sud, Y., and G. K. Walker, 1999: Microphysics of Clouds with the Relaxed Arakawa Schubert Scheme (McRAS). Part I: Design and Evaluation with GATE Phase III Data, 3196-3220.

Sundqvist, H., 1988: Parameterization of condensation and associated clouds in models for weather prediction and general circulation simulation. *Physically Based Modelling and Simulation of Climate and Climatic Change*, M. E. Schlesinger, Ed., Reidel, 433 461.

Tokioka, T., K. Yamazaki, A. Kitoh, and T. Ose, 1988: The equatorial 30-60 day oscillation and the Arakawa-Schubert penetrative cumulus parameterization. *J. Meteor. Soc. Japan*, 66, 883-901.

Wheeler, M., and G. N. Kiladis, 1999: Convectively coupled equatorial waves: Analysis of clouds and temperature in wavenumber-frequency domain. *J. Atmos. Sci.*, **56**, 374-399.

Wu, X., X.-Z. Liang, and G. J. Zhang, 2003: Seasonal migration of ITCZ precipitation across the equator: Why can't GCMs simulate it? *Geophys. Res. Lett*, **30**, 10.1029/2003GL017198.

Xie, P., and P. Arkin, 1997: Global precipitation, a 17-year monthly analysis based on gauge observations, satellite estimates and numerical model outputs. *Bull. Am. Met. Soc.*, **78**, 2539-2558.

Zhang, C. 2001: Double ITCZs. *J. Geophys. Res.*, **106**, 11,785-11,792.

Zhang, G. J., and H. R. Cho, 1991: Parameterization of the vertical transport of momentum by cumulus clouds. Part I: Theory. *J. Atmos. Sci.*, **48**, 1483-1492.

Zhang, M. H. and co-authors, 2004: Comparing clouds and their seasonal variations in 10 atmospheric general circulation models with satellite measurements (in preparation).

Zhou, J., Y. C. Sud and K.-M. Lau, 1996: Impact of orographically induced gravity-wave drag in the GLA GCM. *Quart. J. Roy. Meteor. Soc.*, **122**, 903-927.

Received _____

Exp. Designation	Re-evaporation setting	Remarks	r	var
B1	weak		0.70	1.52
B2	moderate		0.81	1.21
B3	strong		0.80	1.33
H1	strong	Redistributed evap. cooling		
M1	weak	Diffusive CMT		
M2	moderate	Diffusive CMT		

Table 1: Summary of experiments performed. First column gives short hand designation. Second column gives indicates strength of re-evaporation. Third column indicates additional modifications to physical parameterizations. Fourth column gives pattern correlation of simulated precipitation with the CMAP climatology for a 7-season JJA 1981-87 mean.

Exp.	Domain	$\mathcal{P}_0$ mm d^{-1}	$\int \mathcal{R}$ (mm d^{-1})	$\mathcal{P}_0+\int \mathcal{R}$	$\int \mathcal{R}/\mathcal{P}_0$		E_0	$E_0-\mathcal{P}_0$
B1	SITCZ	6.157	3.220	9.376	0.5230	0.3434	5.429	-0.728
"	NITCZ	5.445	2.614	8.059	0.4801	0.3244	4.496	-0.949
"	WAFR	5.122	4.301	9.423	0.8399	0.4565	3.235	-1.887
"	SWUS	0.712	1.451	2.163	2.0367	0.6707	1.155	0.443
B2	SITCZ	4.804	6.801	11.605	1.4156	0.5860	5.402	0.598
"	NITCZ	5.066	5.863	10.929	1.1574	0.5365	4.687	-0.379
"	WAFR	4.575	7.335	11.910	1.6035	0.6159	2.554	-2.021
"	SWUS	0.525	2.730	3.256	5.1954	0.8386	0.894	0.368
B3	SITCZ	3.989	8.233	12.222	2.0640	0.6736	5.282	1.293
"	NITCZ	4.808	8.224	13.031	1.7106	0.6311	4.938	0.130
"	WAFR	3.944	8.436	12.379	2.1388	0.6814	2.349	-1.595
"	SWUS	0.479	2.761	3.240	5.7653	0.8522	0.762	0.283
H1	SITCZ	6.678	12.955	19.632	1.9400	0.6599	5.374	-1.304
"	NITCZ	4.574	8.943	13.517	1.9554	0.6616	4.972	0.399
"	WAFR	5.005	16.965	21.970	3.3899	0.7722	2.734	-2.270
"	SWUS	0.672	5.075	5.747	7.5466	0.8830	1.059	0.387
CMAP	SITCZ	4.636						
"	NITCZ	4.730						
"	WAFR	3.756						
"	SWUS	1.237						

Table 2: Domain averaged precipitation, re-evaporation and related quantities in 4 boxes illustrated in Figure 4 for JJA 1984-85. First column gives experiment designation from Table 1. Second column indicates Box for averages. Third column gives average precipitation $\mathcal{P}_0$ in mm d^{-1}. The fourth column gives the mass weighted vertical integral of moistening due to re-evaporation of falling precipitation, denoted by $\int \mathcal{R}$. This quantity is units of mm d^{-1} and represents the additional rain that would reach the surface if not removed by re-evaporation. The fifth column is the sum $\mathcal{P}_0+\int \mathcal{R}$, that is, the total precipitating condensate generated by autoconversion within a column. Columns 6 and 7 are ratios of $\int \mathcal{R}$ to $\mathcal{P}_0$ and $\int \mathcal{R}+\mathcal{P}_0$ respectively. Column 8 gives the average surface evaporation E_0 in units of mm d^{-1}. The 9-th column is the difference $E_0-\mathcal{P}_0$. Positive numbers in this column indicate that the Box in question exports water horizontally to the rest of the atmosphere, while negative numbers mean water vapor must be imported to supply an excess of precipitation. The last 4 rows, labeled "CMAP", give the observed precipitation in each box.

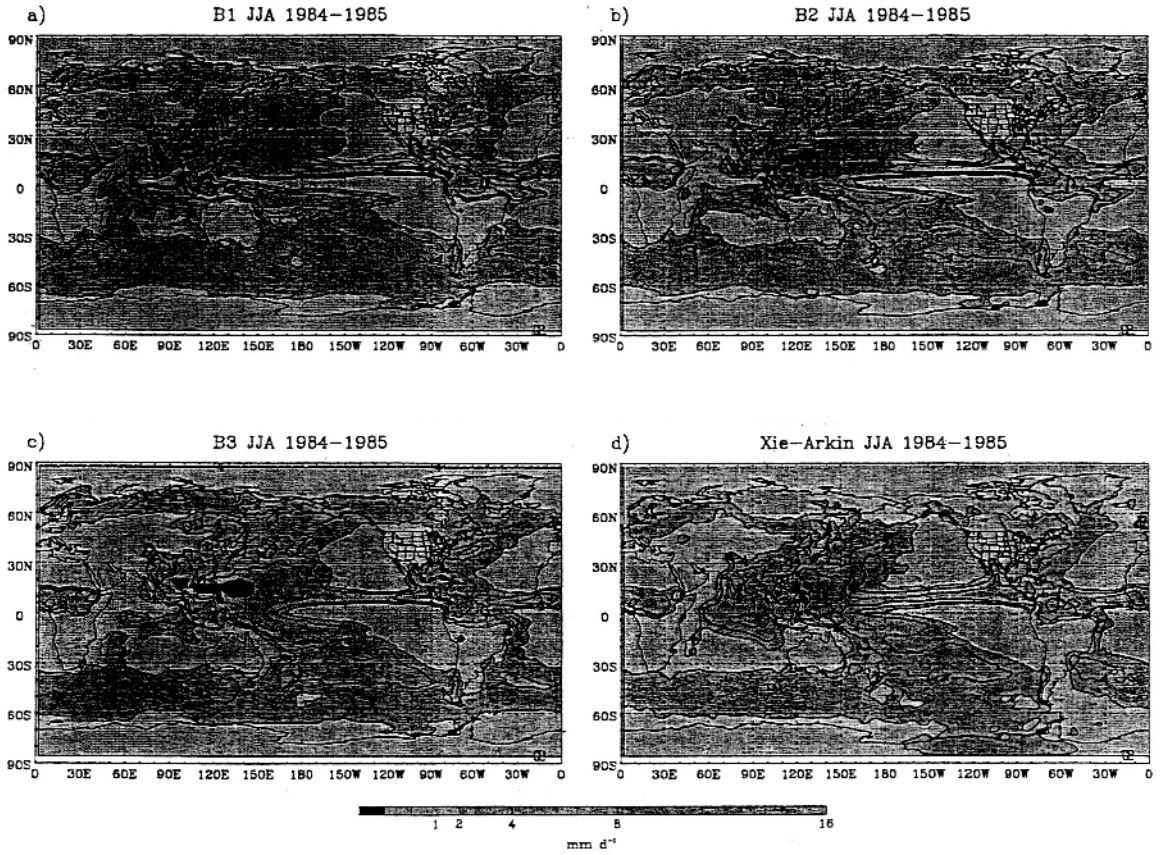

Figure 1: June-August (JJA) averages of precipitation for 1984-85: a) from Experiment B1 with weak re-evaporation, contours are drawn for 1.0, 2.0,, 4.0, 8.0, and 16.0 mm d^{-1} ; b) as (a) except for Experiment B2 (moderate re-evaporation); c) as (a) except for Experiment B3 (strong re-evaporation); d) as (a) except for Xie-Arkin precipitation data.

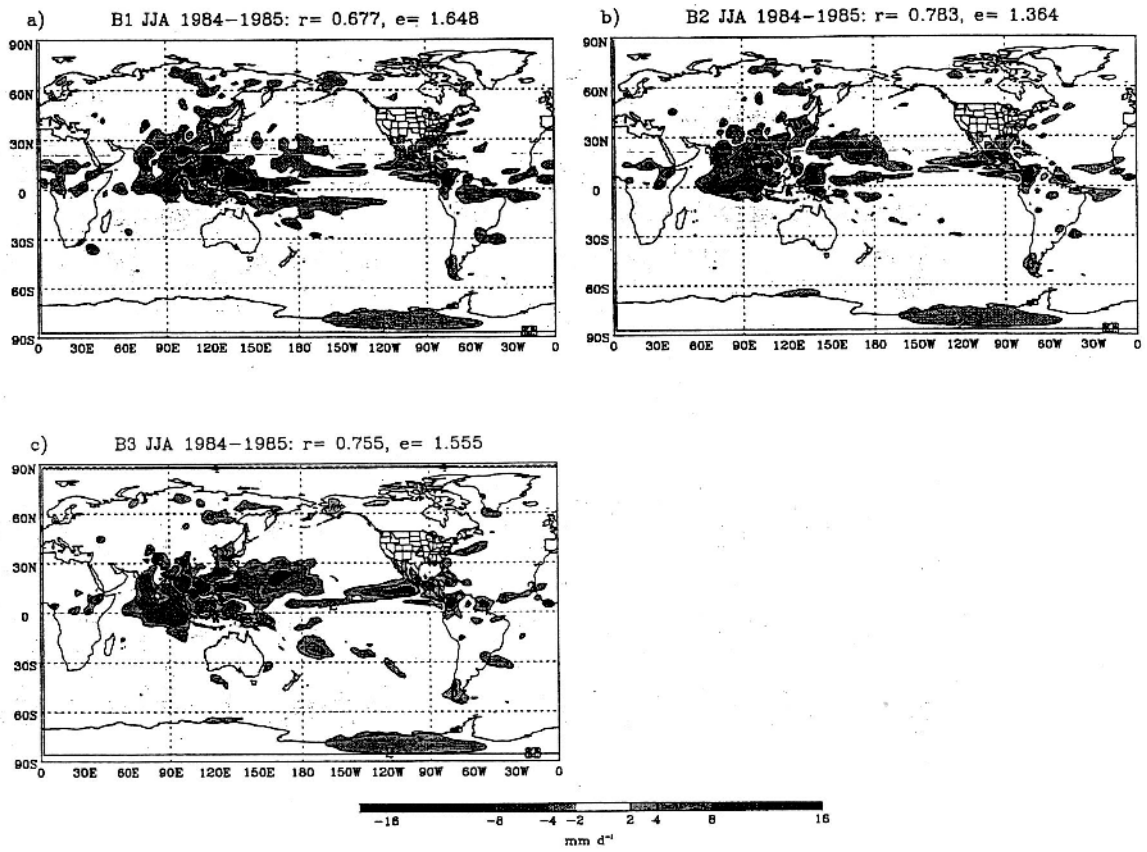

Figure 2: June-August (JJA) average precipitation biases with respect to Xie-Arkin (CMAP) climatology for 1984-85: a) Experiment B1 with weak re-evaporation, contours are drawn for -16, -8, -4,-2, 2, 4, 8, and 16 mm d^{-1} ; b) as (a) except for Experiment B2 (moderate re-evaporation); c) as (a) except for Experiment B3 (strong re-evaporation); d) as (a) except for Xie-Arkin precipitation data.

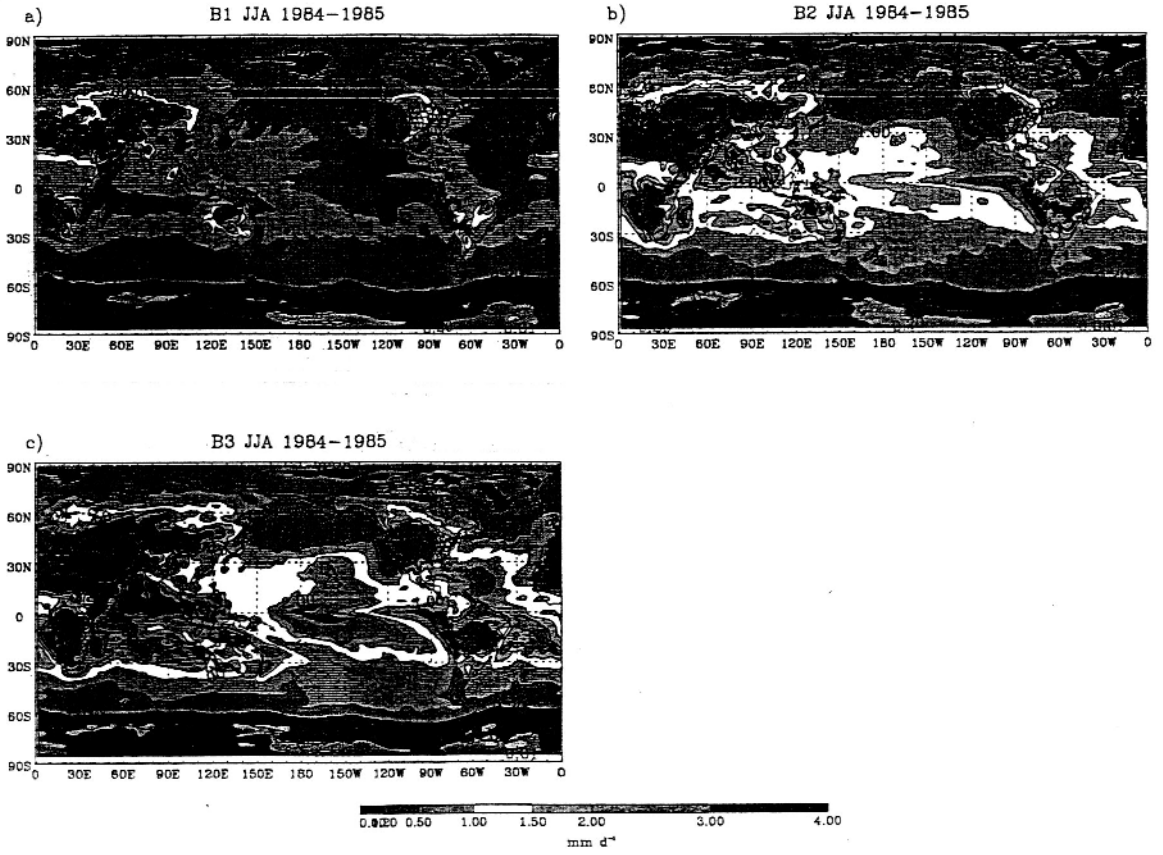

Figure 3: Ratio of re-evaporated precipitation to precipitation reaching the surface, seasonal means for JJA 1984-85: a) B1, weak re-evaporation; b) B2, moderate re-evaporation; and c) B3 strong re-evaporation.

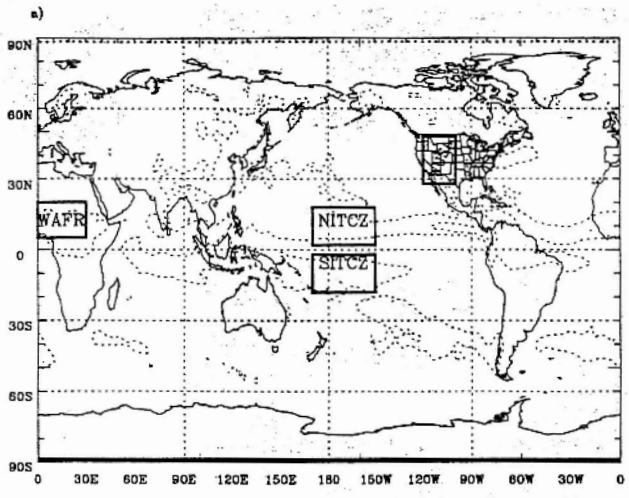

Figure 4: Boxes used in domain average analyses

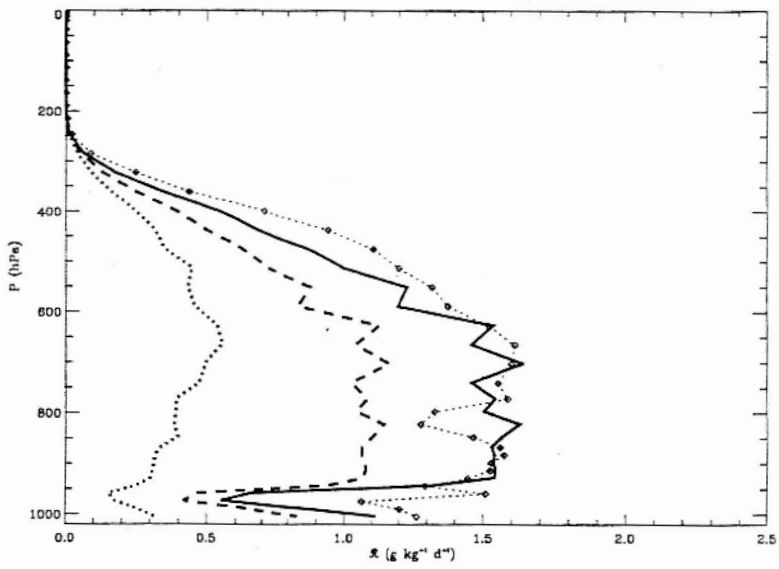

Figure 5: Mean profile of re-evaporation moistening $\mathcal{R}$ for JJA 1984-85 in Box NITCZ. Solid line shows result for Exp B3 (strong $\mathcal{R}$), dashed line for B2 (moderate $\mathcal{R}$), dotted line for B1 (weak $\mathcal{R}$), and open diamonds for H1 (strong $\mathcal{R}$ modified cooling profile).

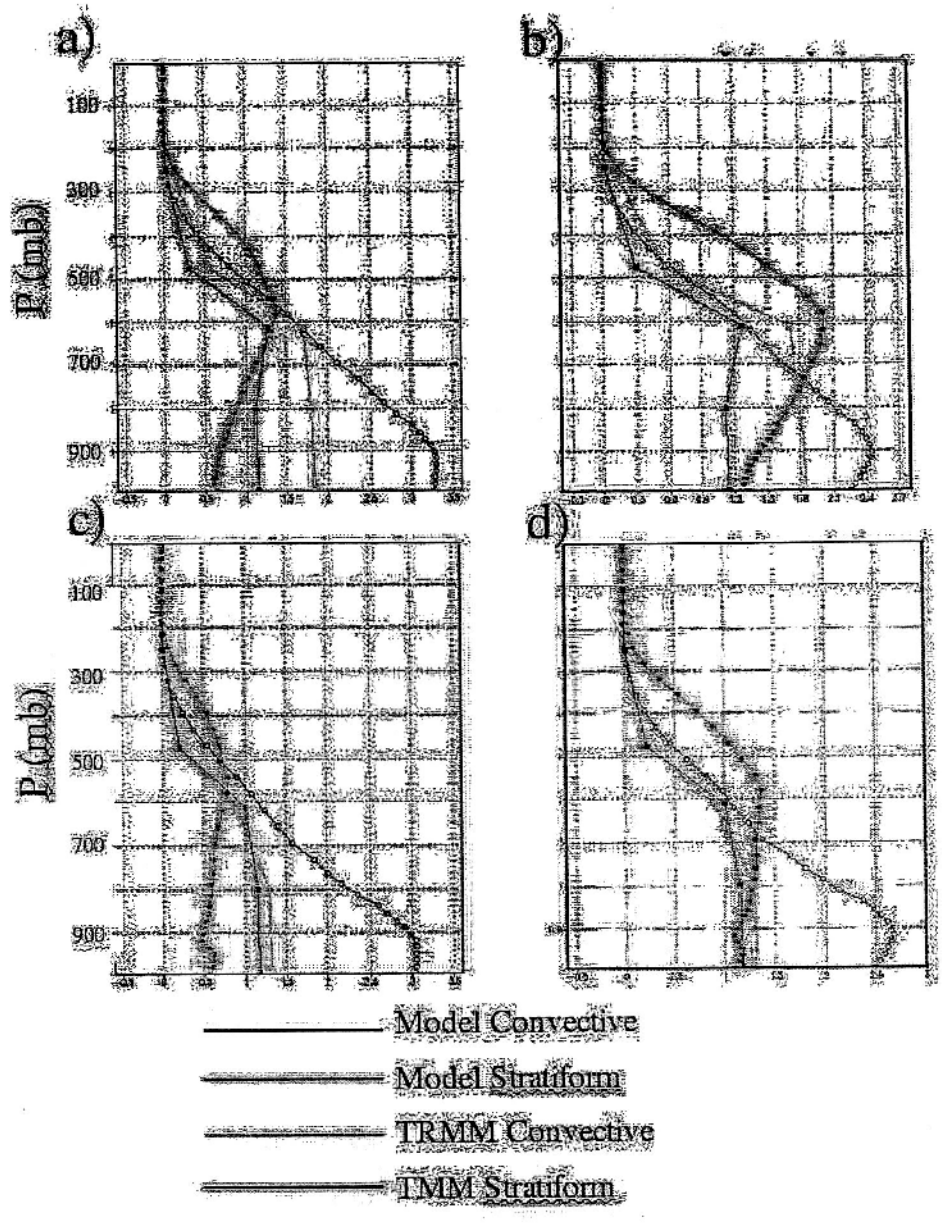

Figure 6: Profiles of tropical (30°S to 30°N) precipitation flux from model experiments, shown in green (stratiform) and blue (convective), and TRMM PR measurements, shown in red (stratiform) and orange (convective). (a) B1 Land mean; (b) B2 land mean; (c)B1 Ocean mean; (d) B2 Ocean mean. Note variations in range of horizontal axis.

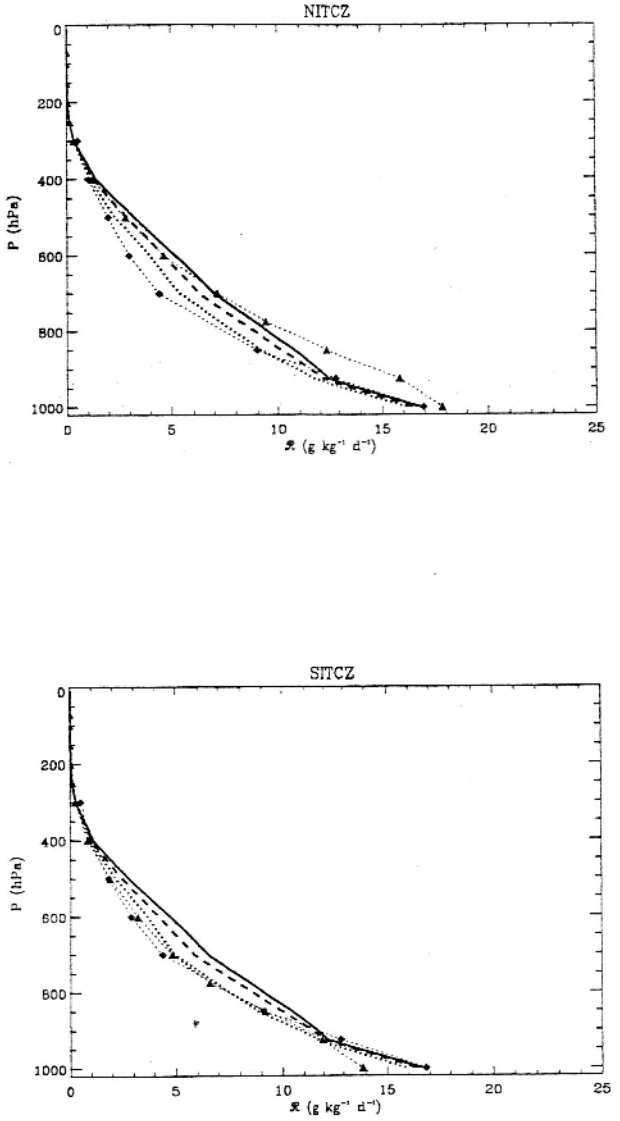

Figure 7: Specific humidity q as a function of pressure in Boxes NITCZ (top) and SITCZ (bottom). Profiles are averages for JJA 1984/85. Solid lines show result for Exp B3, dashed lines for B2 and dotted lines for B1. Filled triangles show the ERA40 re-analysis q-profiles, and filled diamonds show q for the NCEP re-analysis.

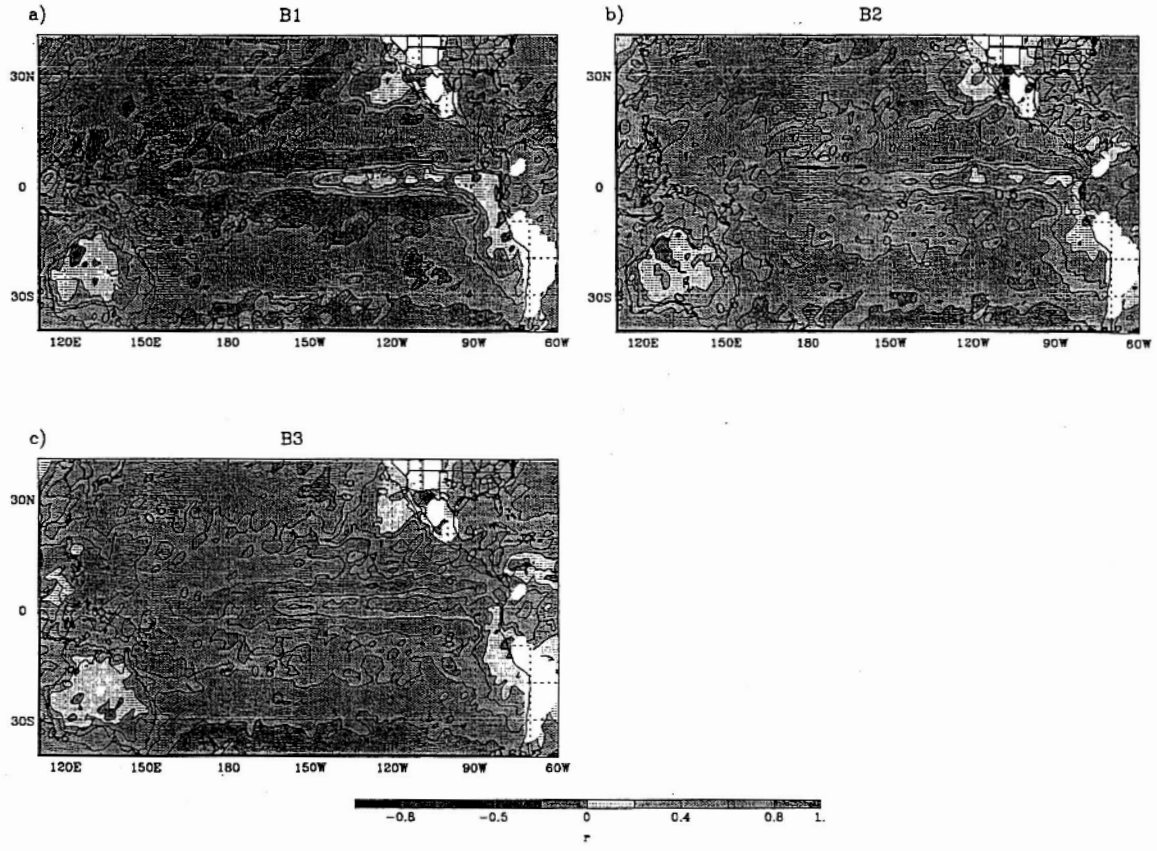

Figure 8: Correlation of daily ω_{850} and $\mathcal{P}_0$ time-series for April 1-Sept. 30 1984 and 1985: (a) for Exp B1 (weak re-evap.); (b) Exp B2; and (c) Exp B3

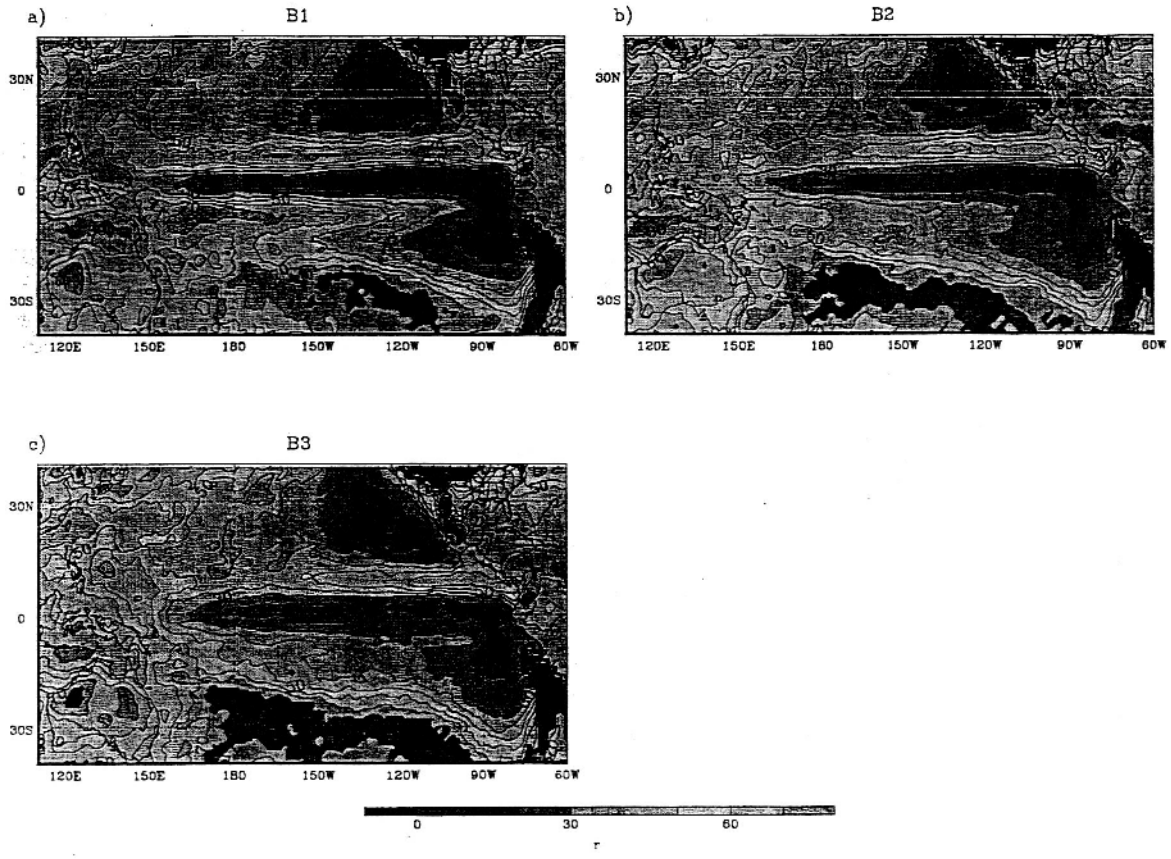

Figure 9: RMS value of daily ω_{850} fluctuations for April 1-Sept. 30 1984 and 1985: (a) for Exp B1 (weak re-evap.); (b) Exp B2; and (c) Exp B3. Units are hPa d^{-1}.

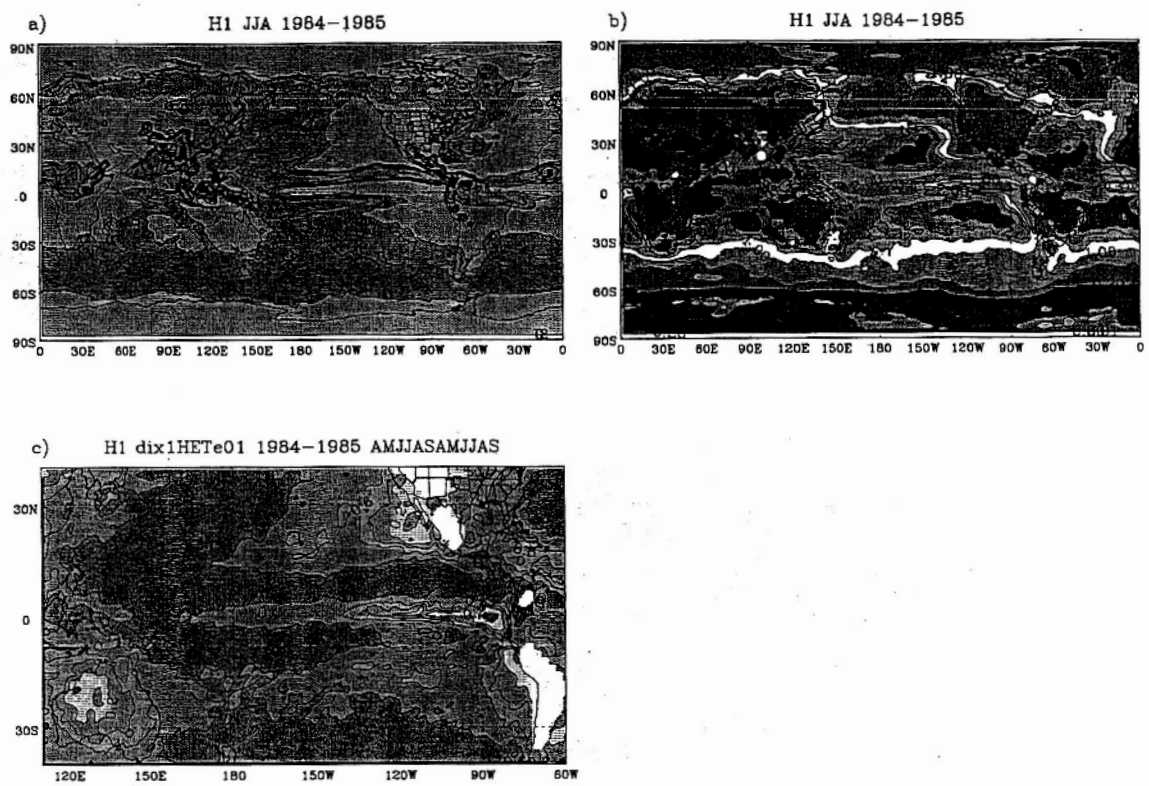

Figure 10: (a) Seasonal mean JJA 1984-85 precipitation for Exp H1; (b) fraction of re-evaporated rain to surface rain; and (c) Correlation of daily ω_{850} and $\mathcal{P}_0$ time-series for April 1-Sept. 30 1984 and 1985

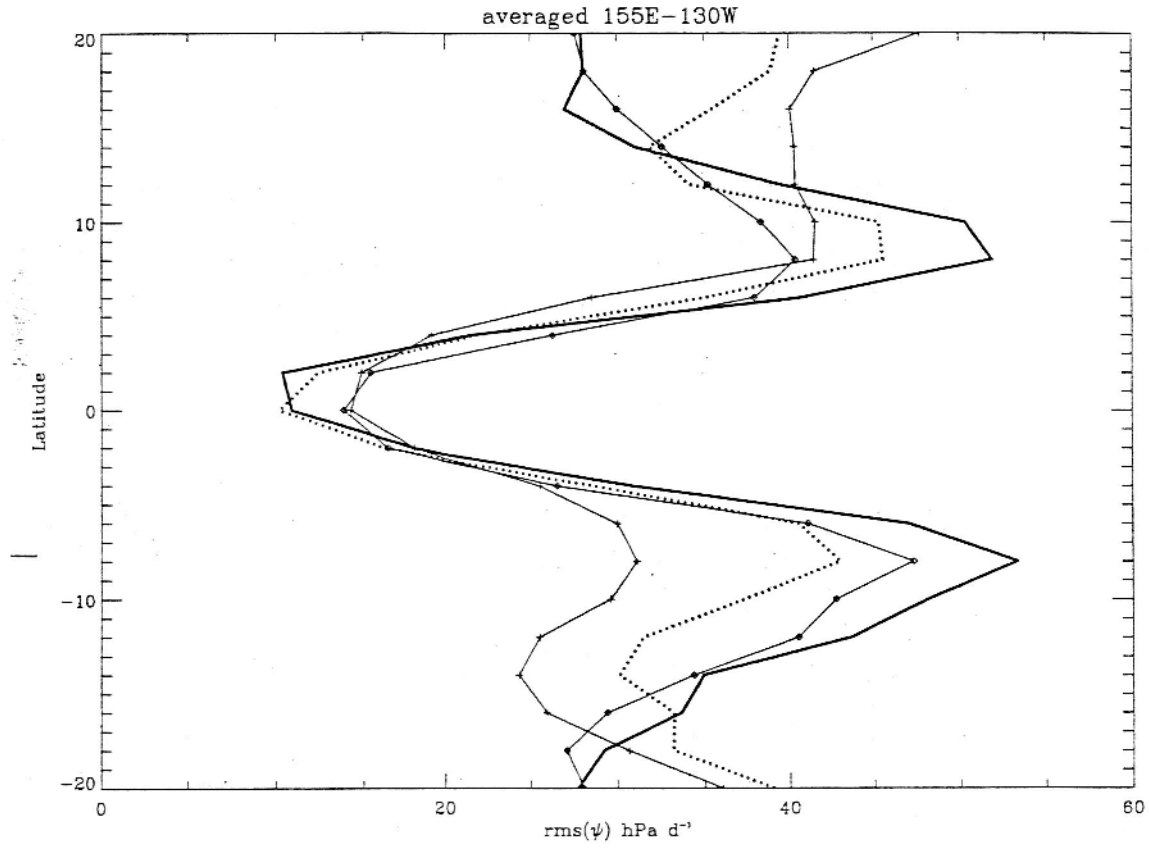

Figure 11: Zonally-averaged RMS value of daily ω_{850} fluctuations between 155°E and 130°W for JJA 1984-85. Thick solid line shows result for Exp B1, dotted line for B2, small diamonds for M1, and small triangle for M2.

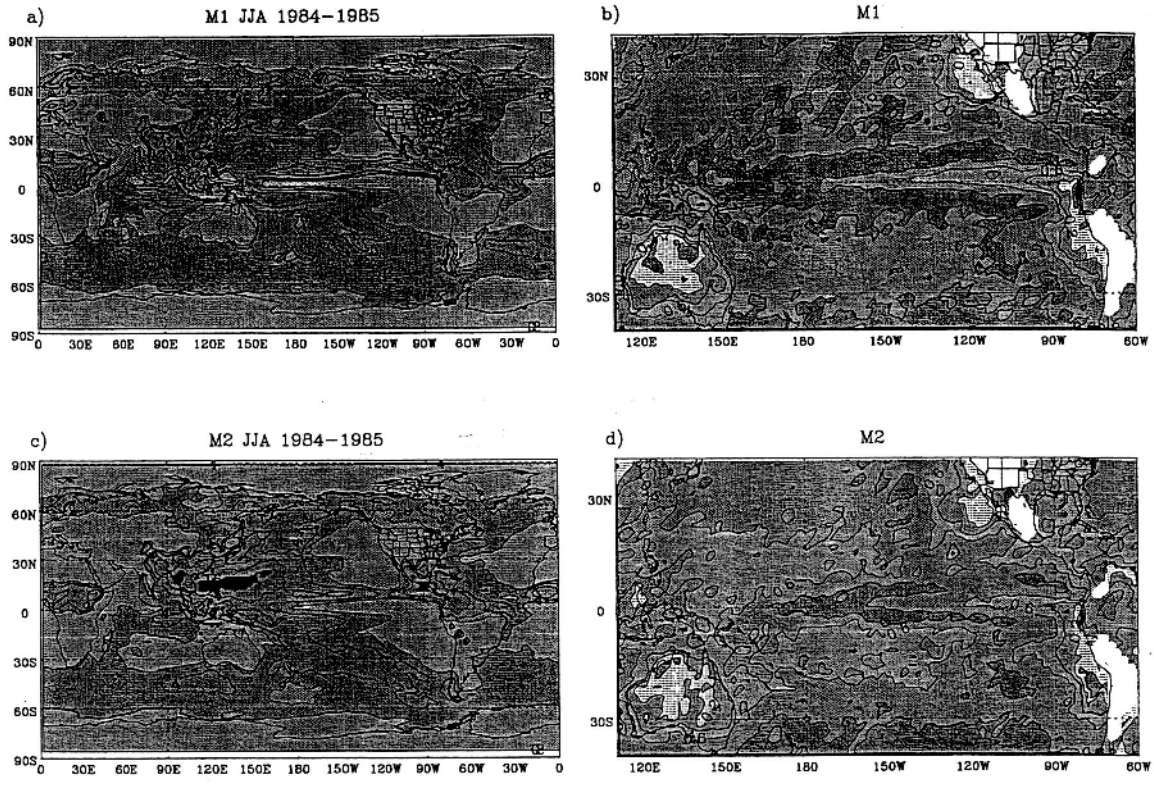

Figure 12: (a) JJA 1984-85 precipitation for Exp M1. (b) Correlation of daily ω_{850} and $\mathcal{P}_0$ time-series for April 1-Sept. 30 1984 and 1985 in Exp M1 (c) as (a) for Exp M2. (d) as (b) for Exp M2

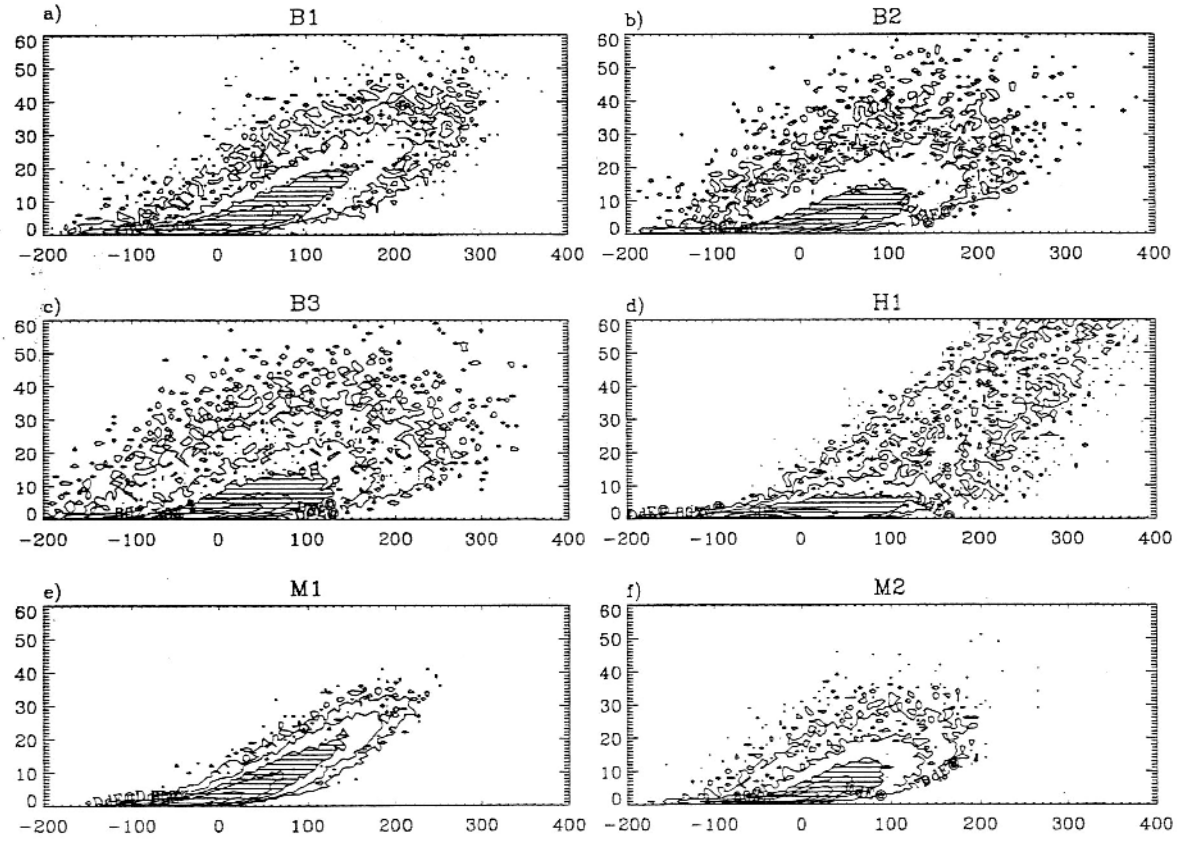

Figure 13: Joint PDFs of daily ω_{850} and $\mathcal{P}_0$ values for all gridpoints within Box SITCZ (Fig.4) for all 6 experiments.

POPULAR SUMMARY

Rain re-evaporation, boundary layer convection interactions, and Pacific rainfall patterns in an AGCM

(Paper to be submitted to Journal of Atmospheric Sciences)

Julio T. Bacmeister, Max J. Suarez, and Franklin R. Robertson

The "double ITCZ bias" is a common and long-standing problem in computer models of the global climate. Models with this problem form two bands of intense rain, known as intertropical convergence zones or "ITCZs', on either side of the Equator, near 10S and 10N, for most of the year. In nature, there is usually a single band of intense rain north of the Equator (near 10N), with only rare instances of a second southern ITCZ. The cause of the double ITCZ bias is not well understood. However, in our climate model we find a relationship between evaporation of falling rain and the strength of the double ITCZ bias. Rain evaporation is a small-scale process that is not directly simulated in climate models, and so must be estimated or "parameterized" in some fashion using available model fields. In our model the tendency to form double ITCZs depends on whether rain evaporation is assumed to an efficient process or an inefficient one. With efficient rain evaporation the double ITCZ bias is reduced. We track this sensitivity to the connection between convection and air motion near the surface. Normally, convection and surface motions are tightly coupled in climate models. Rain evaporation causes strong cooling of the atmosphere near the surface, which tends to disrupt air flow into convective regions. This reduces positive feedbacks between convection and moisture transport. It appears that such feedbacks, if too strong, can lead to the double ITCZ bias.